Lattice distortions in layered type arsenides LnTAs$_2$ (Ln=La–Nd, Sm, Gd, Tb; T=Ag, Au): Crystal structures, electronic and magnetic properties

D. Rutzinger [a], C. Bartsch [a], M. Doerr [b], H. Rosner [c], V. Neu [d], Th. Doert [a,*], M. Ruck [a]

[a] Anorganische Chemie, Fachrichtung Chemie und Lebensmittelchemie, Technische Universität Dresden, D-01062 Dresden, Germany
[b] Institut für Festkörperphysik, Technische Universität Dresden, D-01062 Dresden, Germany
[c] Max-Planck-Institut für Chemische Physik fester Stoffe, Nöthnitzer Str. 40, D-01187 Dresden, Germany
[d] IFW Dresden, Institut für metallische Werkstoffe, Helmholtzstr. 20, D-01069 Dresden, Germany

ARTICLE INFO

ABSTRACT

The lanthanide coinage-metal diarsenides LnTAs$_2$ (Ln=La, Ce–Nd, Sm; T=Ag, Au) have been reinvestigated and their structures have been refined from single crystal X-ray data. Two different distortion variants of the HfCuSi$_2$ type are found: PrAgAs$_2$, NdAgAs$_2$, SmAgAs$_2$, GdAgAs$_2$, TbAgAs$_2$, NdAuAs$_2$ and SmAuAs$_2$ crystallize as twofold superstructures in space group $Pmcn$ with the As atoms of their planar layers forming zigzag chains, whereas LaAgAs$_2$, CeAgAs$_2$ and PrAuAs$_2$ adopt a fourfold superstructure (space group $Pmca$) with cis-trans chains of As atoms. The respective atomic positions can be derived from the HfCuSi$_2$ type by group-subgroup relations. The compounds with zigzag chains of As atoms exhibit metallic behaviour while those with cis-trans chains are semiconducting as measured on powder pellets. The majority of the compounds including $4f$ elements show antiferromagnetic ordering at $T_N < 20$ K.

© 2010 Elsevier Inc. All rights reserved.

1. Introduction

Compounds with layered type structures are subject of intensive investigations due to both interesting structural features and physical properties. Among these, binary and ternary compounds of the compositions MT_4, MT_2X_2, MTX_2, $MT_{1 \pm \delta}X_2$ and MX_2 have been investigated (M=alkaline, alkaline earth or rare earth element, T=d-block element, X=element of group 13–15) [1–8]. Numerous compounds of the general composition MTX_2 adopt the HfCuSi$_2$ type [8–19] or one of its distorted variants [20,21]. HfCuSi$_2$ crystallizes in the tetragonal space group $P4/nmm$ (No. 129) [9] with eight atoms in the unit cell (a=3.732(4) Å, c=8.99(1) Å). Characteristic feature of the HfCuSi$_2$ structure are PbO-like layers formed by the Cu and Si1 atoms and square planar nets of the Si2 atoms. These motives are separated by Hf atoms, which are embedded in the hollows of the CuSi layers (Fig. 1, left). In the ternary lanthanide compounds LnTAs$_2$ the lanthanide atoms Ln, the coinage metal atoms T, and the arsenic atoms occupy the Hf, Cu and Si positions, respectively.

Similar structural motifs can be found in the iron-based layered superconductors LaFePO [22], LaFeAsO [23] and its derivatives (cf. [24,25] e.g.), which crystallize in the ZrCuSiAs

type [26] (Fig. 1, right). Contrary to the HfCuSi$_2$ type, Zr is shifted towards Si resulting in the formation of an additional PbO-like layer.

Due to local $Peierls$-like distortions in the planar layers of arsenic atoms in the LnTAs$_2$ compounds (Ln=Y, La, Ce–Nd, Sm, Gd–Lu; T=Cu, Ag, Au), these atoms have been found to be symmetry breaking and their positions cannot be described by tetragonal symmetry [13,14,21]. Some of the LnAgAs$_2$ and LnAuAs$_2$ compounds have been described as commensurate superstructures of the HfCuSi$_2$ type in the orthorhombic space group $Pmcn$ (No. 62), others in the $P4/nmm$ subcell [20], although only the structure model for PrAgAs$_2$ is based on single crystal data. The compounds crystallizing in space group $Pmcn$ are twofold superstructures with lattice parameters a_0, b_0 and $2c_0$ with respect to the HfCuSi$_2$ type. In contrast to the results published by Eschen and Jeitschko [20], Demchyna et al. identified another type of distortion for CeAgAs$_2$, which crystallizes as a fourfold superstructure in space group $Pmca$ (No. 57) with lattice parameters $\sqrt{2} a_0$, $\sqrt{2} b_0$ and $2 c_0$. This compound comprises cis-trans chains of the As atoms of the planar layer [21].

Since considerable interest is directed towards the structures and physical properties of layered type rare-earth metal – transition metal – arsenides, investigations on LnAgAs$_2$ (Ln=La, Ce–Nd, Sm, Gd, Tb) and LnAuAs$_2$ (Ln=Pr, Nd, Sm) compounds were performed. The results are presented in the following.

* Corresponding author. Fax: +49 351 463 37287.
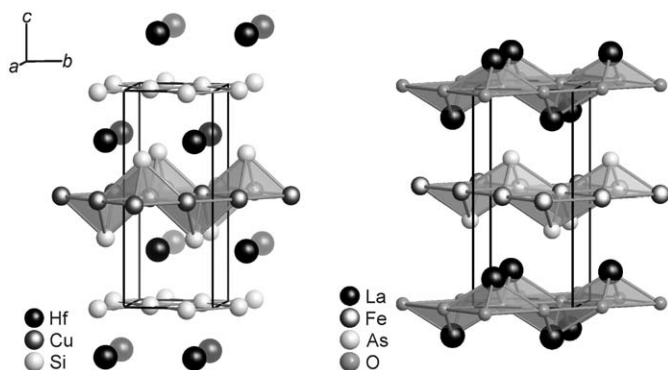E-mail address: thomas.doert@chemie.tu-dresden.de (Th. Doert).

Fig. 1. Structural relationship of the HfCuSi$_2$ type (left) and LaFeAsO (right, both in space group $P4/nmm$, No. 129).

2. Experimental

2.1. Synthesis

The preparations were carried out in an argon-filled glove box (M. Braun, $p(O_2) \leqslant 1$ ppm, $p(H_2O) \leqslant 1$ ppm, argon purification with molecular sieve and copper catalyst). Pieces of lanthanum, cerium, praseodymium, neodymium (all 99.9%, Treibacher AG), samarium (99.9%, Chempur GmbH), gadolinium (99.9%, ABCR) or terbium (99.9%, Acros) freshly filed from rods of the respective rare earth metals, silver (powder, 99.9%, Chempur GmbH) or gold (powder, 99.9+%, Chempur GmbH), and arsenic (powder, > 99.997% metal based, Aldrich; As$_2$O$_3$ removed by sublimation prior to use) were mixed in the atomic ratio of 1:1:2. The reactions were carried out in a sixfold excess of a LiCl/KCl flux (LiCl, KCl: powders, p.a, Merck, dried at 410 K in dynamic vacuum prior to use) in glassy carbon crucibles, which were sealed in evacuated silica tubes. The samples were heated up to 1023 K for 48 h, annealed for 96 h, and cooled to 623 K during 192 h. The flux was removed with water and the products were washed with ethanol. Air stable, shiny black platelets of the target compounds were obtained.

2.2. X-ray investigations

Powder samples of the reaction products were measured on a Stadi P diffractometer (Stoe & Cie., Darmstadt, Cu $K\alpha_1$, Ge monochromator) and characterized with the WinXPow program package [27]. Buerger precession photographs (Zr-filtered Mo radiation, imaging plate system) were taken in order to check the quality of the crystals and to determine the lattice parameters and the reflection conditions. Data sets were recorded on an imaging plate diffraction system (IPDS I or IPDS II, both Stoe & Cie., Darmstadt, Mo $K\alpha$ radiation, graphite monochromator). The descriptions of the habitus of the platelets were optimized using sets of symmetrically equivalent reflections [28,29]. Data reduction included Lorentz- and polarization factor corrections and numerical absorption corrections were applied using the refined crystal shape [28] and the structure models were refined with SHELX97 [30].

2.3. Electrical conductivity

The temperature dependent ($20\,K \leqslant T \leqslant 310\,K$) resistivity was studied by a four-probe method on pressed and sintered cylindrical samples (pellets) with 8 mm diameter and 2 mm height, approximately. Silver paste was used as contacting agent to prepare four contacts in linear geometry. Since the samples were sintered at 523 K from ground polycrystals, the density of the material is not known exactly and therefore the geometry coefficient could be estimated only. After preparation, all measurements were performed under vacuum conditions in a two-stage Gifford–McMahon refrigerator with a temperature sweep rate of $2\,K\,min^{-1}$. Dependent on the resistivity of the sample at room temperature, a measuring current between 10 µA for compounds with semiconducting character and 100 mA for those with metallic behavior was chosen.

2.4. Band structure calculations

Density functional band structure calculations using a full potential all-electron local orbital code FPLO (version fplo8.00–31) [31,32] within the local (spin) density approximation (L(S)DA) were performed including spin-orbit coupling. The Perdew–Wang [33] parameterization of the exchange-correlation potential is employed. Density of states (DOS) and band structures were calculated after convergence of the total energy on a dense k-mesh with $12 \times 12 \times 12$ points. The strong Coulomb repulsion in the Pr $4f$ orbitals are treated on a mean field level using the LSDA+U approximation in the atomic-limit double counting scheme [34,35]. The results presented below use the LSDA+U method [36] in the rotationally invariant form [37], as a representative value, $U=8$ eV was chosen. A variation of U between 6 and 10 eV does not significantly influence the relevant valence states. The experimental structural parameters have been used throughout the calculations.

2.5. Magnetization experiments

Powders of randomly oriented small crystallites were loosely embedded into a cylindrical form with diluted glue. The samples were measured in a Quantum Design physical properties measurement system (PPMS) with vibrating sample magnetometer (VSM) option in fields up to 9 T and in a temperature range from 2 to 300 K. Hysteresis loops were conducted with a field sweep rate of $0.02\,T\,min^{-1}$ and temperature dependent magnetization measurements were performed at a fixed field of $\mu_0 H = 0.25$ T with a temperature sweep rate of $2\,K\,min^{-1}$.

3. Results and discussion

3.1. X-ray investigations

3.1.1. Powder patterns

Powder diffraction data of the reaction products revealed that the La, Ce, Pr, Nd and Sm compounds were obtained as single-phase samples at a reaction temperature of 1023 K, GdAgAs$_2$ and TbAgAs$_2$ were accompanied with a considerable amount of the respective binary lanthanide arsenide LnAs and elemental silver. The X-ray powder diffraction patterns are shown in Fig. 2 for SmAuAs$_2$ as representative for the compounds crystallizing in a twofold superstructure and in Fig. 3 for LaAgAs$_2$ representing a compound crystallizing in a fourfold superstructure of the HfCuSi$_2$ type. The cell parameters as well as the volume per formula unit obtained from the powder data are summarized in Table 1. Crystals of GdAgAs$_2$ and TbAgAs$_2$ for single crystal X-ray investigations could be selected manually from the multiphase reaction mixtures.

The powder diffractograms show broadening or splitting of some reflections at higher 2θ angles, e.g. reflections 0 2 0 and 2 0 0 at $2\theta \approx 45°$ or reflections 1 3 4 and 3 1 4 at $2\theta \approx 77°$ for SmAuAs$_2$, and reflections 4 2 4 and 2 4 4 at $2\theta \approx 75°$ for LaAgAs$_2$. This
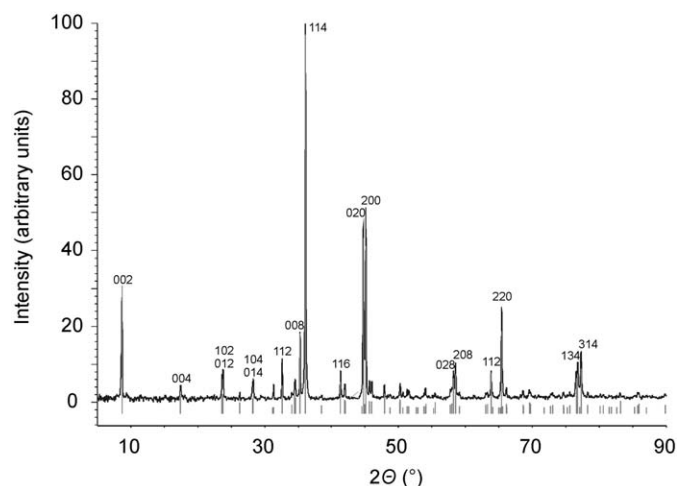
Fig. 2. X-ray powder diffraction pattern of $SmAuAs_2$ and calculated peaks in space group $Pmcn$ (No. 62, twofold superstructure).
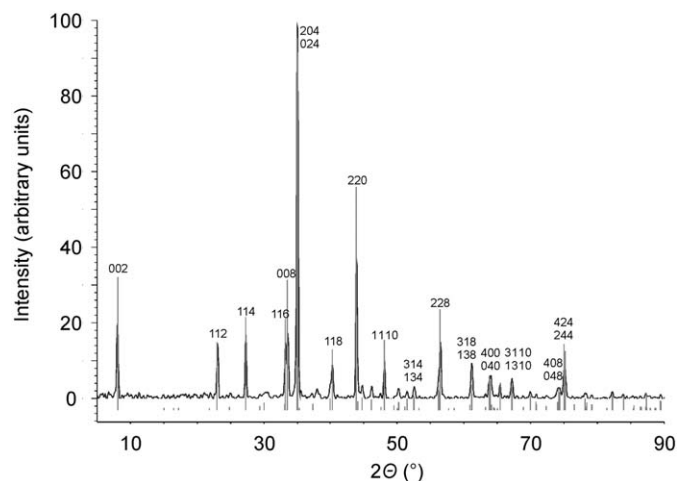

Fig. 3. X-ray powder diffraction pattern of $LaAgAs_2$ and calculated peaks in space group $Pmca$ (No. 57, fourfold superstructure).

Table 1
Cell parameters (Å), no. of formula units per unit cell and volume ($Å^3$) per formula unit of the $LnTAs_2$ compounds.

Compound	a	b	c	V	Z	V/Z
$LaAgAs_2$	5.801(2)	5.814(2)	21.219(4)	715.5(3)	8	89.44
$CeAgAs_2$	5.771(2)	5.775(2)	21.081(4)	702.6(2)	8	87.82
$PrAgAs_2$	4.017(1)	4.062(1)	21.027(4)	343.1(1)	4	85.85
$NdAgAs_2$	4.032(1)	4.032(1)	20.977(4)	341.0(1)	4	85.26
$SmAgAs_2$	3.995(1)	4.013(1)	20.872(1)	333.1(1)	4	83.64
$GdAgAs_2$	3.973(1)	3.976(1)	20.841(3)	329.3(1)	4	82.32
$TbAgAs_2$	3.956(1)	3.955(1)	20.748(1)	324.6(1)	4	81.15
$PrAuAs_2$	5.766(2)	5.757(2)	20.458(4)	679.1(2)	8	84.88
$NdAuAs_2$	4.058(1)	4.059(1)	20.435(4)	336.6(1)	4	84.15
$SmAuAs_2$	4.019(1)	4.049(1)	20.331(4)	330.9(1)	4	82.72

indicates a distortion of the tetragonal cell of the aristotype for both types of superstructures.

3.1.2. Single crystal structure determinations

Precession records of $LaAgAs_2$, $CeAgAs_2$ and $PrAuAs_2$ revealed a (pseudo-)tetragonal unit cell with $a \approx b \approx 5.8\,Å$ ($\sqrt{2} \times 4\,Å$) and $c \approx 21\,Å$. Records of $PrAgAs_2$, $NdAgAs_2$, $SmAgAs_2$, $GdAgAs_2$ and

$TbAgAs_2$ as well as those of $NdAuAs_2$ and $SmAuAs_2$ show a unit cell with $a \approx b \approx 4\,Å$ and $c \approx 20.5\,Å$.

Based on the main reflections of the single-crystal diffraction data, a model of the average structure was developed for $SmAuAs_2$ in $P4/nmm$ (No. 129, Fig. 4) using the atomic positions of the $HfCuSi_2$ type as a starting point. In this structure, the results of the refinement match those obtained by Eschen and Jeitschko [20]. The most striking features of the structure are the exceptional large thermal displacement parameters observed for the As2 atoms in the arsenic layers.

Analysis of the single crystal data for $PrAgAs_2$, $NdAgAs_2$, $SmAgAs_2$, $GdAgAs_2$, $TbAgAs_2$, $NdAuAs_2$ and $SmAuAs_2$ revealed a twofold superstructure ($a' = a_0$, $b' = b_0$, $c' = 2c_0$) of the aristotype with Laue symmetry mmm. Space group $Pmcn$ (No. 62, non-standard setting of $Pnma$) was identified following the Bärnighausen formalism [38,39] stated in Fig. 5. Non-standard settings were chosen to emphasize the structural relationship with the tetragonal aristotype (layer stacking along [001]). The Wyckoff positions, atomic coordinates and displacement parameters are listed in Table 2, final results of the refinements as well as relevant crystallographic data can be found in Table 3, interatomic distances and angles of the As2 atoms are stated in Table 4.

In an analogous way, space group $Pmca$ (No. 57, non-standard setting of $Pbcm$) was identified for the fourfold superstructures following the Bärnighausen formalism stated in Fig. 6. The Wyckoff positions, atomic coordinates and displacement parameters are listed in Table 5, final results of the refinements as well as relevant crystallographic data can be found in Table 6, interatomic distances and angles of the As3 atoms are stated in Table 7.

Contrary to the respective early $LnCuAs_2$ (Ln = La, Ce, Pr, Nd, Sm), which have been reported in literature to crystallize with an excess of copper (from $LaCu_{1.24}As_2$ to $SmCu_{1.05}As_2$) [8,18] and an undistorted arsenic layer, the silver and gold compounds investigated here crystallize with an 1:1:2 molar ratio or, in case of $CeAuAs_2$, with a slight deficiency of gold [40].

In both types of superstructures, the Ln atoms are surrounded by square antiprisms of As atoms of the PbO-like layer and As atoms of the distorted planar layers leading to three different Ln–As distances. The As atoms of the planar layers are surrounded by a square antiprism of Ln and T atoms, the As atoms of the arsenic layer by four As atoms and four Ln atoms. The latter
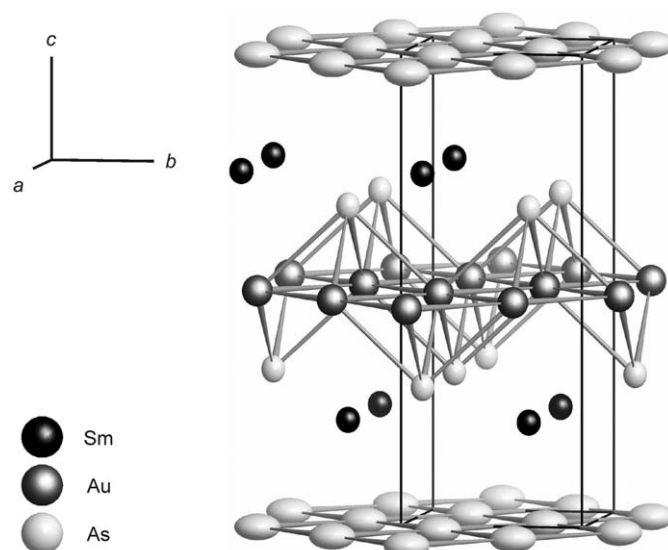

Fig. 4. Average structure for $SmAuAs_2$ in $P4/nmm$, ellipsoids at the 99% probability level.

motive can be described as a (4+4) coordination, set up by a compressed tetrahedron of Ln atoms and a rectangle of As atoms around the central As atom (Fig. 7, left). A (4+4+4) coordination is realized for the T atoms consisting of two interpenetrating elongated tetrahedra of Ln or As atoms and a square of T atoms (Fig. 7, right).
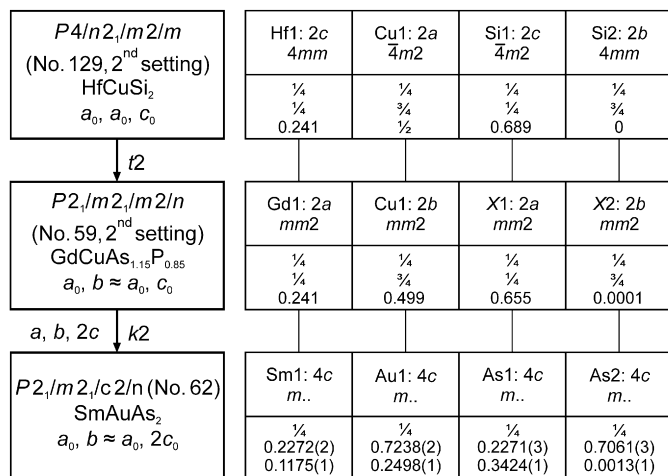
The main difference between the undistorted aristotype and the distorted compounds is found in the planar layer of the main group elements Si and As, respectively. In accordance with crystal structure and magnetic data (vide infra), the formula of the title compounds can be written as $Ln^{3+}T^+As^{3-}As^-$, where the As^{3-} are found in the puckered [LnAs] slabs and the As^- atoms in the planar layers. Following the Zintl–Klemm concept the As^- atoms with 6 valence electrons should be two-bonded due to their pseudo-chalcogen character. This is realized in the $LnTAs_2$ compounds by the formation of planar $^1_\infty$[As] chains.

In the case of the twofold superstructures, infinite zigzag chains of the As2 atoms along [010] are found (Fig. 8). This comes along with an orthorhombic deformation of the $HfCuSi_2$ structure. The doubling of the c-axis is due to a shift of $\Delta x = \Delta y = 0.5$ of the As2 atoms in alternating layers in $z \approx 0$ and $z \approx 0.5$. The superposition of both shifts is the origin of the exceptional large anisotropic displacement parameters of the As2 atoms in the $P4/nmm$ average structure.

In the case of the fourfold superstructures, infinite cis-trans chains of the As3 atoms along [010] are formed (Fig. 9), which results in the $\sqrt{2}\,a \times \sqrt{2}\,b$ enlargement of the orthorhombic unit cell. The doubling along c is in this case caused by a shift of $\Delta y = 0.5$, which corresponds to an inverse orientation of the cis-trans chains in $z \approx 0$ and $z \approx 0.5$.

The As–As distances in the undistorted $HfCuSi_2$ type structure depend on the tetragonal lattice parameter a only: $As–As = a/\sqrt{2}$. The distances change gradually within one series of coinage metal compounds and adopt average values of approximately 2.82 Å for the silver and 2.90 Å for the gold compounds. Both distortions of the square-planar As layers described above lead to a considerable

$P4/n\,2_1/m\,2/m$ (No. 129, 2nd setting) $HfCuSi_2$ a_0, a_0, c_0	Hf1: 2c 4mm	Cu1: 2a $\bar{4}m2$	Si1: 2c $\bar{4}m2$	Si2: 2b 4mm
	¼ ¼ 0.241	¼ ¾ ½	¼ ¼ 0.689	¼ ¾ 0

↓ t2

$P2_1/m\,2_1/m\,2/n$ (No. 59, 2nd setting) $GdCuAs_{1.15}P_{0.85}$ $a_0, b \approx a_0, c_0$	Gd1: 2a mm2	Cu1: 2b mm2	X1: 2a mm2	X2: 2b mm2
	¼ ¼ 0.241	¼ ¾ 0.499	¼ ¼ 0.655	¼ ¾ 0.0001

a, b, 2c ↓ k2

$P2_1/m\,2_1/c\,2/n$ (No. 62) $SmAuAs_2$ $a_0, b \approx a_0, 2c_0$	Sm1: 4c m..	Au1: 4c m..	As1: 4c m..	As2: 4c m..
	¼ 0.2272(2) 0.1175(1)	¼ 0.7238(2) 0.2498(1)	¼ 0.2271(3) 0.3424(1)	¼ 0.7061(3) 0.0013(1)

Fig. 5. Bärnighausen tree for the symmetry relation between the $HfCuSi_2$ ($P4/nmm$) and the $SmAuAs_2$ structure (Pmcn). Note that the atomic positions of the $HfCuSi_2$ type are shifted by $z+1/2$ with respect to the data given in the original publication [9].

Table 2
Wyckoff sites, atomic coordinates and coefficients U_{ij}^* of the tensors of the anisotropic displacement parameters (Å²) for $PrAgAs_2$, $NdAgAs_2$, $SmAgAs_2$, $GdAgAs_2$, $TbAgAs_2$, $NdAuAs_2$ and $SmAuAs_2$ in Pmcn.

Atom	Site	x	y	z	U_{11}	U_{22}	U_{33}	U_{23}
Pr	4c	1/4	0.2257(2)	0.1157(1)	0.0080(6)	0.0041(5)	0.0054(4)	0.0001(3)
Ag	4c	1/4	0.7241(3)	0.2502(1)	0.0126(8)	0.0069(6)	0.0097(6)	−0.0011(4)
As1	4c	1/4	0.2244(3)	0.3388(1)	0.0095(10)	0.0028(7)	0.0068(8)	−0.0001(5)
As2	4c	1/4	0.7018(4)	0.0015(8)	0.0109(11)	0.0078(7)	0.0060(8)	0.0002(6)
Nd	4c	1/4	0.2278(3)	0.1154(1)	0.0120(9)	0.0047(7)	0.0045(4)	0.0002(3)
Ag	4c	1/4	0.7263(3)	0.2499(4)	0.0138(13)	0.0109(10)	0.0078(5)	−0.0001(9)
As1	4c	1/4	0.2274(4)	0.3396(1)	0.0124(18)	0.0053(15)	0.0071(7)	−0.0001(5)
As2	4c	1/4	0.7045(4)	0.0010(3)	0.0121(12)	0.0115(9)	0.0052(8)	−0.0035(14)
Sm	4c	1/4	0.2377(3)	0.1149(1)	0.0036(11)	0.0100(13)	0.0071(3)	−0.0004
Ag	4c	1/4	0.7388(4)	0.2500(3)	0.013(2)	0.009(2)	0.0108(4)	−0.0003(7)
As1	4c	1/4	0.2383(5)	0.3411(1)	0.006(3)	0.007(3)	0.0086(6)	−0.0009(7)
As2	4c	1/4	0.7255(6)	0.0017(4)	0.019(2)	0.019(2)	0.0057(8)	0.0001(13)
Gd	4c	1/4	0.2297(2)	0.1144(1)	0.0112(4)	0.0088(3)	0.0122(2)	0.0000(2)
Ag	4c	1/4	0.7295(2)	0.2498(2)	0.0153(5)	0.0128(4)	0.0168(3)	−0.0003(3)
As1	4c	1/4	0.2299(2)	0.3420(1)	0.0133(7)	0.0080(5)	0.0137(4)	0.0004(2)
As2	4c	1/4	0.7087(2)	0.0016(2)	0.0128(5)	0.0117(3)	0.0117(4)	−0.0003(6)
Tb	4c	1/4	0.2321(5)	0.1141(1)	0.0082(17)	0.0014(15)	0.0022(4)	0.0005(5)
Ag	4c	1/4	0.7291(7)	0.2502(5)	0.011(3)	0.006(2)	0.0067(6)	0.0008(11)
As1	4c	1/4	0.2307(8)	0.3429(1)	0.001(4)	0.007(3)	0.0031(8)	−0.0005(11)
As2	4c	1/4	0.7097(8)	0.0016(5)	0.005(3)	0.007(2)	0.0016(11)	−0.0008(18)
Nd	4c	1/4	0.2279(3)	0.1177(1)	0.0008(11)	0.0031(11)	0.0047(7)	−0.0003(3)
Au	4c	1/4	0.7253(2)	0.2504(2)	0.0119(10)	0.0136(8)	0.0117(6)	0.0012(6)
As1	4c	1/4	0.2276(3)	0.3400(1)		$U_{iso}=0.0029(5)$ **		
As2	4c	1/4	0.7097(5)	0.0020(5)	0.0125(15)	0.0087(12)	0.0043(13)	0.002(2)
Sm	4c	1/4	0.2272(2)	0.1175(1)	0.0079(5)	0.0027(4)	0.0055(4)	0.0001(2)
Au	4c	1/4	0.7238(2)	0.2498(1)	0.0163(5)	0.0102(3)	0.0125(4)	−0.0001(2)
As1	4c	1/4	0.2271(3)	0.3424(1)	0.0065(9)	0.0024(6)	0.0087(8)	0.0002(5)
As2	4c	1/4	0.7061(3)	0.0013(1)	0.0114(11)	0.0059(7)	0.0057(8)	−0.0012(5)

$^*U_{12}=U_{23}=0$; ** isotropic refinement.

Table 3
Crystallographic and refinement data for $PrAgAs_2$, $NdAgAs_2$, $SmAgAs_2$, $GdAgAs_2$, $TbAgAs_2$, $NdAuAs_2$ and $SmAuAs_2$ in *Pmcn*.

	$PrAgAs_2$	$NdAgAs_2$	$SmAgAs_2$	$GdAgAs_2$	$TbAgAs_2$	$NdAuAs_2$	$SmAuA_2$
Chemical formula	$PrAgAs_2$	$NdAgAs_2$	$SmAgAs_2$	$GdAgAs_2$	$TbAgAs_2$	$NdAuAs_2$	$SmAuA_2$
CSD number	420611	420612	420613	420614	420615	420631	420632
Formula weight (g mol^{-1})	398.62	401.95	408.06	414.96	416,63	491.05	497.16
Space group	*Pnma*	*Pnma*	*Pnma*	*Pnma*	*Pnma*	*Pnma*	*Pnma*
a (Å)	4.017(1)	4.032(1)	3.995(1)	3.973(1)	3.956(1)	4.058(1)	4.019(1)
b (Å)	4.062(1)	4.032(1)	4.013(1)	3.976(1)	3.955(1)	4.059(1)	4.049(1)
c (Å)	21.027(4)	20.977(4)	20.872(1)	20.842(2)	20.841(3)	20.435(4)	20.331(4)
V (Å^3)	343.1(2)	341.0(2)	333.1(2)	329.28(7)	324.6(1)	336.6(2)	330.9(1)
Z	4	4	4	4	4	4	4
ρ_x (g cm^{-3})	7.72	7.83	8.14	8.37	8.52	9.69	9.98
Crystal size (µm^3)	$49 \times 41 \times 6$	$45 \times 28 \times 27$	$108 \times 95 \times 4$	$180 \times 160 \times 17$	$85 \times 60 \times 3$	$212 \times 199 \times 12$	$163 \times 140 \times 10$
Radiation, λ				Mo $K\alpha$, 0.71073 Å			
diffractometer	IPDS I	IPDS I	IPDS I	IPDS II	IPDS I	IPDS I	IPDS I
T_{min}, T_{max}	0.245, 0.790	0.343, 0.446	0.188, 0.932	0.030, 0.458	0.238, 0.940	0.013, 0.393	0.043, 0.796
θ range (°)	$2.91 \leq \theta \leq 25.72$	$2.90 \leq \theta \leq 25.75$	$2.94 \leq \theta \leq 25.71$	$2.93 \leq \theta \leq 33.35$	$1.96 \leq \theta \leq 25.66$	$1.99 \leq \theta \leq 25.63$	$2.00 \leq \theta \leq 25.76$
Range of $h\,k\,l$	$-4 \leq h, k \leq 4$	$-4 \leq h, k \leq 4$	$-4 \leq h \leq 4$	$-6 \leq h, k \leq 6$	$-4 \leq h, k \leq 4$	$-4 \leq h, k \leq 4$	$-4 \leq h, k \leq 4$
	$-25 \leq l \leq 25$	$-23 \leq l \leq 24$	$-25 \leq l \leq 25$	$-32 \leq l \leq 28$	$-25 \leq l \leq 25$	$-24 \leq l \leq 24$	$-24 \leq l \leq 24$
Measured reflections	3568	3491	3477	6539	3392	3453	3436
Independent reflections	398	387	392	769	384	373	337
Observed reflections	300	321	302	678	284	346	296
Refined parameters	27	27	27	27	26	24	26
R_{int}	0.087	0.060	0.053	0.050	0.090	0.079	0.041
R_1	0.033	0.022	0.023	0.030	0.034	0.034	0.026
$wR_2(I>3\sigma)$	0.075	0.052	0.045	0.074	0.068	0.087	0.059
S (all I)	1.04	1.11	1.10	1.07	1.03	1.07	1.00
$\Delta\rho_{max}$, $\Delta\rho_{min}$ (e$^-$Å^{-3})	2.26, −2.06	2.00, −1.48	1.91, −1.41	1.95, −2.31	2.52, −2.09	2.15, −2.68	1.71, −1.72
Twin volume fractions	0.95, 0.05	0.54, 0.46	0.53, 0.47	0.44, 0.56	0.54, 0.46	0.52, 0.48	–

Table 4
Interatomic distances and angles of the As2 atoms for $PrAgAs_2$, $NdAgAs_2$, $SmAgAs_2$, $GdAgAs_2$, $TbAgAs_2$, $NdAuAs_2$ and $SmAuAs_2$ in *Pmcn*.

	$PrAgAs_2$	$NdAgAs_2$	$SmAgAs_2$	$GdAgAs_2$	$TbAgAs_2$	$NdAuAs_2$	$SmAuAs_2$
ic	2.593(2)	2.605(2)	2.696(2)	2.590(1)	2.582(3)	2.650(2)	2.613(1)
bc	3.148(2)	3.122(2)	2.974(2)	3.053(1)	3.031(3)	3.111(2)	3.115(1)
angle	101.52(6)	101.4(2)	95.6(2)	100.21(9)	100.0(3)	99.9(3)	100.55(5)

With ic: distances in the chains, bc: shortest distances between the chains, angle: angle between As2 atoms within the chains.
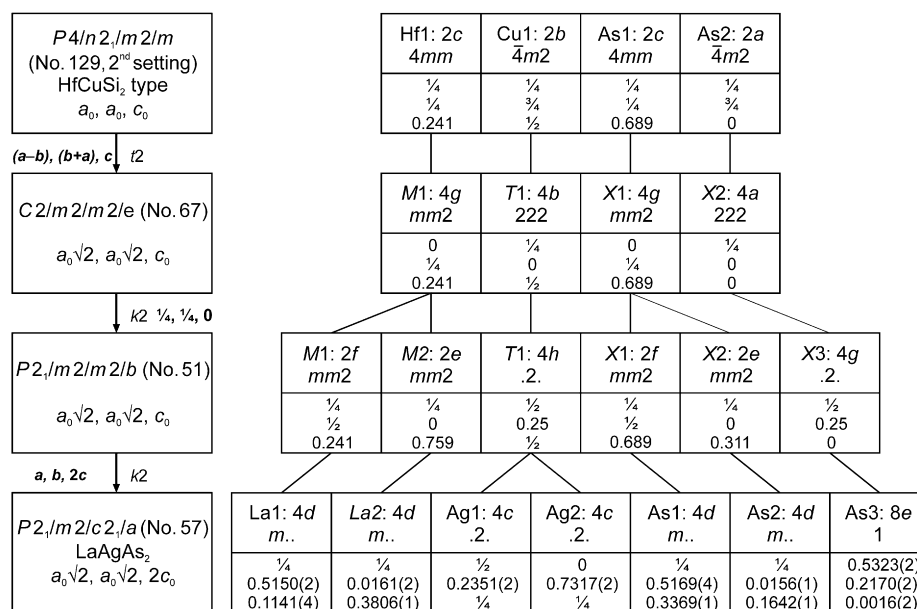

Fig. 6. *Bärnighausen* tree for the symmetry relation between the HfCuSi$_2$ ($P4/nmm$) and the LaAgAs$_2$ structure (*Pmca*). Note that the atomic positions of the HfCuSi$_2$ type are shifted by $z+1/2$ with respect to the data given in the original publication [9].

Table 5

Wyckoff sites, atomic coordinates and coefficients U_{ij} of the tensors of the anisotropic displacement parameter (Å^2) for $LaAgAs_2$, $CeAgAs_2$ and $PrAuAs_2$ in $Pmca$.

| Atom	Site	x	y	z	U_{11}	U_{22}	U_{33}	U_{12}	U_{13}	U_{23}
La1	4d	1/4	0.5150(2)	0.6142(1)	0.0039(7)	0.0031(5)	0.0047(5)	0	0	0.0014(5)
La2	4d	1/4	0.0161(2)	0.8806(1)	0.0036(7)	0.0037(5)	0.0052(5)	0	0	0.0004(5)
Ag1	4c	1/2	0.2351(2)	1/4	0.010(2)	0.006(1)	0.009(1)	0	0.0006(7)	0
Ag2	4c	1/2	0.7317(2)	1/4	0.006(2)	0.0083(9)	0.010(1)	0	0.0001(7)	0
As1	4d	1/4	0.5169(4)	0.8369(1)	0.005(1)	0.0035(8)	0.0066(9)	0	0	0.0003(9)
As2	4d	1/4	0.0156(4)	0.6642(1)	0.005(1)	0.0033(8)	0.0078(9)	0	0	0.0013(9)
As3	8e	0.5323(2)	0.2170(2)	0.0016(2)	0.0061(5)	0.0070(4)	0.0062(5)	0.0001(4)	−0.0006(7)	0.0009(7)
Ce1	4d	1/4	0.5130(2)	0.6135(1)	0.0049(7)	0.0042(6)	0.0097(8)	0	0	−0.0007(4)
Ce2	4d	1/4	0.0141(2)	0.8821(1)	0.0047(7)	0.0037(7)	0.0088(8)	0	0	−0.0007(4)
Ag1	4c	1/2	0.2372(2)	1/4	0.009(2)	0.008(1)	0.012(2)	0	0.0011(7)	0
Ag2	4c	1/2	0.7341(2)	1/4	0.008(2)	0.010(1)	0.011(1)	0	0.0012(7)	0
As1	4d	1/4	0.5136(3)	0.8386(1)	0.004(1)	0.005(1)	0.012(1)	0	0	−0.0004(8)
As2	4d	1/4	0.0142(3)	0.6623(1)	0.007(1)	0.004(1)	0.009(1)	0	0	−0.0007(8)
As3	8e	0.5283(2)	0.2216(2)	0.0009(2)	0.0083(5)	0.0089(5)	0.0095(7)	0.0003(4)	−0.0006(8)	−0.0007(8)
Pr1	4d	1/4	0.5145(2)	0.6159(1)	0.0028(9)	0.0024(8)	0.0029(7)	0	0	0.0004(5)
Pr2	4d	1/4	0.0158(2)	0.8797(4)	0.0026(9)	0.0019(8)	0.0030(8)	0	0	0.0004(5)
Au1	4c	1/2	0.2345(1)	1/4	0.014(1)	0.0121(7)	0.0105(8)	0	0.0003(4)	0
Au2	4c	1/2	0.7310(2)	1/4	0.014(1)	0.0122(6)	0.0112(8)	0	0.0009(4)	0
As1	4d	1/4	0.5153(4)	0.8398(1)	0.006(1)	0.004(1)	0.008(1)	0	0	0.0006(7)
As2	4d	1/4	0.0156(4)	0.6616(1)	0.005(1)	0.004(1)	0.008(1)	0	0	0.0006(7)
As3	8e	0.5302(2)	0.2218(2)	0.0009(2)	0.0052(7)	0.0046(6)	0.0040(7)	−0.0010(5)	−0.0015(9)	−0.0006(8)

Table 6

Crystallographic and refinement data for $LaAgAs_2$, $CeAgAs_2$ and $PrAuAs_2$ in $Pmca$.

	$LaAgAs_2$	$CeAgAs_2$	$PrAuAs_2$
Chemical formula	$LaAgAs_2$	$CeAgAs_2$	$PrAuAs_2$
CSD number	420609	420610	420630
Formula weight (g mol^{-1})	396.62	397.83	487.72
Space group	$Pmca$	$Pmca$	$Pmca$
a (Å)	5.801(2)	5.771(2)	5.766(2)
b (Å)	5.814(2)	5.775(2)	5.757(2)
c (Å)	21.219(4)	21.081(4)	20.458(4)
V (Å^3)	715.5(3)	702.6(2)	679.1(2)
Z	8	8	8
ρ_x (g cm^{-3})	7.36	7.55	9.54
Crystal size (μm^3)	$130 \times 108 \times 5$	$83 \times 46 \times 28$	$144 \times 128 \times 18$
Radiation, λ		Mo $K\alpha$, 0.71073 Å	
Diffractometer	IPDS I	IPDS I	IPDS I
T_{min}, T_{max}	0.148, 0.875	0.226, 0.346	0.041, 0.267
θ range (°)	$1.92 \leq \theta \leq 25.80$	$3.53 \leq \theta \leq 25.85$	$1.99 \leq \theta \leq 25.80$
Range of h k l	$-7 \leq h, k \leq 7$	$-7 \leq h, k \leq 7$	$-7 \leq h, k \leq 7$
	$-25 \leq l \leq 25$	$-24 \leq l \leq 24$	$-25 \leq l \leq 25$
Measured reflections	7552	7336	7130
Independent reflections	832	762	787
Observed reflections	538	552	604
Refined parameters	46	46	46
R_{int}	0.084	0.105	0.053
R_1	0.032	0.033	0.031
$wR_2(I>3\sigma)$	0.056	0.066	0.077
S (all I)	0.99	1.09	1.10
$\Delta\rho_{max}$, $\Delta\rho_{min}$ ($\text{e}^- \text{Å}^{-3}$)	1.57, −1.49	1.59, −1.80	3.92, −2.05
Twin volume fractions	0.83, 0.17	0.61, 0.39	0.41, 0.59

Table 7

Interatomic distances and angles of the As3 atoms for $LaAgAs_2$, $CeAgAs_2$ and $PrAuAs_2$ in $Pmca$.

	$LaAgAs_2$	$CeAgAs_2$	$PrAuAs_2$
a_b	2.526(2)	2.581(2)	2.578(2)
b_{ib}	2.552(1)	2.559(2)	2.535(2)
a_{in}	3.275(2)	3.232(2)	3.222(2)
b_{bc}	3.312(2)	3.212(2)	3.232(2)
Angle (°)	98.44(4)	97.26(4)	97.76(5)

With a and b: crystallographic directions (b in propagation direction of the chains), angle: angle between As3 atoms within the chains, indices: ib=intra-chain bonding, in=intra-chain non bonding, bc=shortest distance between chains.
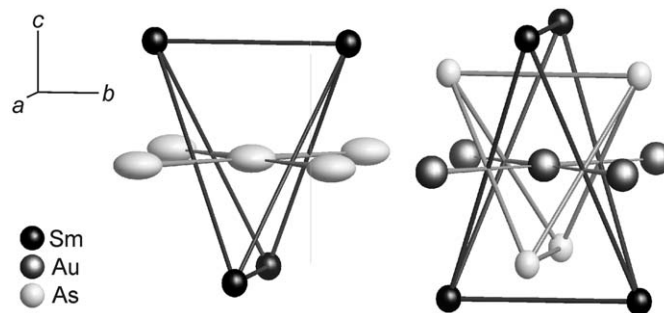
Fig. 7. Coordination polyhedra for the As2 atom (left) and the Au atom (right) of $SmAuAs_2$ in $P4/nmm$, ellipsoids at the 99% probability level.
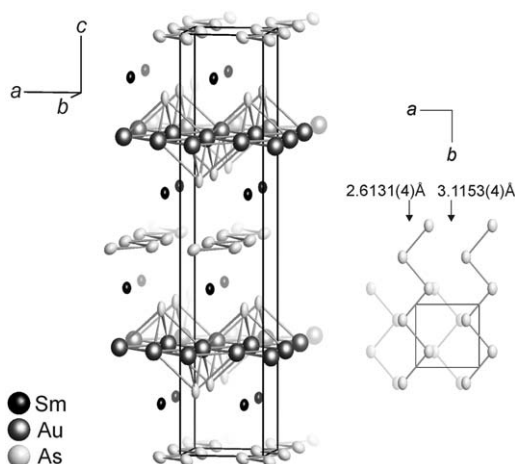
Fig. 8. Structure of SmAuAs$_2$ in *Pmcn* (No. 62), ellipsoids at the 99.9% probability level. Left: complete structure, right: As2 layers along [001] including distances in and between chains.
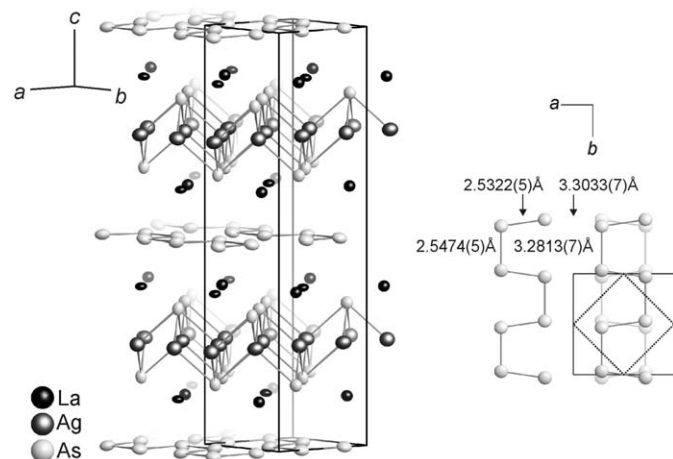

Fig. 9. Structure of LaAgAs$_2$ in *Pmca* (No. 57), ellipsoids at the 99.9% probability level. Left: complete structure, right: As3 layers along [001] including distances in and between chains.

Fig. 10. Course of the volume per formula unit with decreasing ionic radii of the lanthanide metals. Diamonds: silver compounds, circles: gold compounds, empty symbols: incommensurately modulated structures, gray: commensurately modulated structures with cis-trans chains, black: commensurately modulated structures with zigzag chains.

differentiation in the interatomic distances (cf. Tables 4 and 7). Compounds with cis-trans chains in general exhibit smaller intrachain As–As distances than those with zigzag chains. The intrachain distances in the silver *Ln*AgAs$_2$ compounds varies between 2.53 and 2.69 Å, those in the *Ln*Aus$_2$ compounds between 2.54 and 2.65 Å. These distances can be regarded as bonding based on a covalent radius of 1.19 Å for arsenic [41]. Overlap population analyses confirm this assumption but also suggest a minor stabilizing contribution from atom pairs with distances up to about 3.2 Å. In compounds with cis-trans chains, two kinds of these larger distances can be found: interchain distances and 1,4-interchain distances (3.22–3.31 Å). Structures with As zigzag chains show intrachain distances between 2.97 and 3.15 Å, their 1,3-interchain distances are much larger (> 3.9 Å).

Comparable distortion variants to the presented commensurately modulated compounds were found for CeAuAs$_2$ [40], GdCuAs$_2$, GdAuAs$_2$ and TbAuAs$_2$ [42] —the first one crystallizes in an incommensurately modulated structure with cis-trans chains, the latter three in incommensurately modulates structures with zigzag chains. Outlining the course of the volume per formula unit with the ionic radius of the lanthanide elements, an almost linear decrease of the volumes according to the lanthanide contraction becomes visible (Fig. 10).
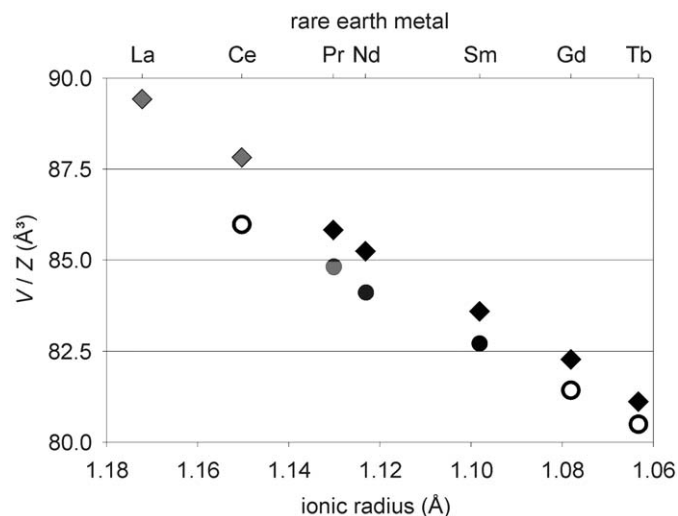
The assignment of the wrong space groups for numerous *Ln*AgAs$_2$ and *Ln*AuAs$_2$ compounds in literature [16,20] may be traced back to the fact that all crystals (despite SmAuAs$_2$ in this study) are twinned along [001] due to the pseudo-tetragonal cell. Consequently, the zonal reflection conditions $h\,0\,l$: $l=2n$ for space group *Pmcn* and $h\,0\,l$: $l=2n$, $h\,k\,0$: $h=2n$ for space group *Pmca* [39] are violated and the determination of the correct space group is hampered. In fact, it can best be accomplished following the *Bärnighausen* formalism.

Further details of the crystal structure investigations can be obtained from the Fachinformationszentrum Karlsruhe, 76344 Eggenstein-Leopoldshafen, Germany (fax: +497247 808 666; e-mail: crysdata@fiz.karlsruhe.de), on quoting the depository numbers CSD-420609 (LaAgAs$_2$), CSD-420610 (CeAgAs$_2$), CSD-420611 (PrAgAs$_2$), CSD-420612 (NdAgAs$_2$), CSD-420613 (SmAgAs$_2$), CSD-420614 (GdAgAs$_2$), CSD-420615 (TbAgAs$_2$), CSD-420630 (PrAuAs$_2$), CSD-420631 (NdAuAs$_2$) and CSD-420632 (SmAuAs$_2$).

3.2. Electrical conductivity and band structure calculation

The electrical conductivity of a number of isostructural compounds of the *Ln*AgAs$_2$ and *Ln*AuAs$_2$ series gives an impression of the influence of the crystal or electronic structure on the macroscopic properties. The character of conductivity shows a great variety, from metallic to (small gap) semiconducting type. This is illustrated by the resistivity curves of CeAgAs$_2$, CeAuAs$_2$ and PrAgAs$_2$ (Figs. 11–13). This selection is mainly motivated by the special behavior of CeCuAs$_2$, for which semiconducting behavior connected with a partial Kondo character of the Ce^{3+} ion was reported in contrast to a metallic character of all other *Ln*CuAs$_2$ compounds [43]. In the presented case, CeAgAs$_2$ and CeAuAs$_2$ (Figs. 11 and 12) are characterized by a negative temperature coefficient of the resistivity. This behavior is in contrast to data found in literature, which show a positive temperature coefficient over a wide temperature range. Nevertheless, it agrees well with the reported properties of CeCuAs$_2$ [43,44]. The absolute values of the resistivity are small, especially in the case of CeAuAs$_2$. This suggests a more or less indifferent character of electrical transport near a change to a metallic system. In addition, the small kink in the resistivity curve
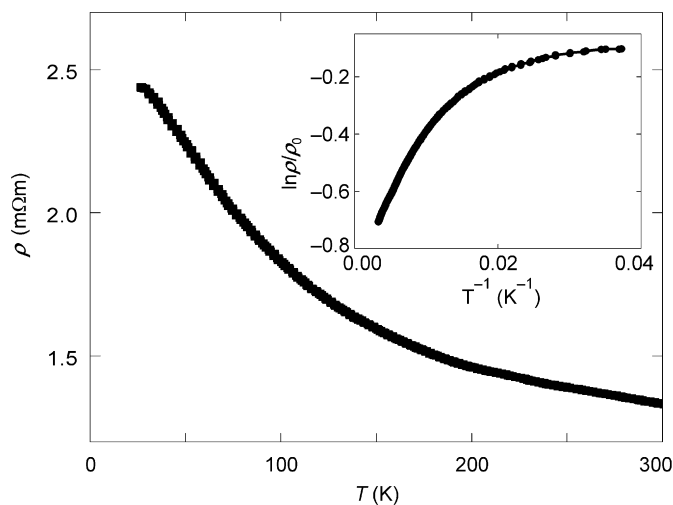
Fig. 11. Temperature dependence of the electrical resistivity of polycrystalline CeAgAs$_2$. The data are an average of one cooling and one heating run (no hysteresis). The inset shows the logarithmic behavior in order to analyze energy scales.
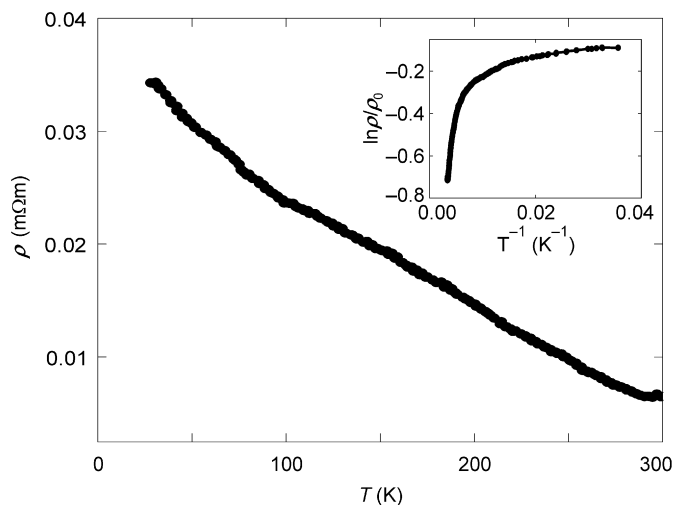

Fig. 13. Temperature dependence of the electrical resistivity of polycrystalline PrAgAs$_2$. The data are an average of one cooling and one heating run (no hysteresis) and show a linear change with temperature.

Fig. 12. Temperature dependence of the electrical resistivity of polycrystalline CeAuAs$_2$. The data are an average of one cooling and one heating run (no hysteresis). The inset shows the logarithmic behavior in order to analyze energy scales.

of CeAuAs$_2$ may be taken as a hint for a structural change as proposed in [44].

One way to analyze the temperature dependence of resistivity is the consideration of the thermal activation of charges taking the Boltzmann factor as the dominant quantity, i.e. $\rho \propto \exp(E_g/2kT)$. With the assumption that both compounds are intrinsic semiconductors the gap energies can be estimated (the $\rho(T^{-1})$ curves are presented as insets of Figs. 11 and 12). The calculated gaps are rather small and seem to be strongly dependent on temperature (1 meV at low temperatures up to 60 meV at high temperatures for CeAgAs$_2$ and 0.2 meV up to 8 meV for CeAuAs$_2$) which is difficult to understand. Therefore, also other models of electrical transport have to taken into consideration. One way is the assumption of a Mott variable range hopping (VRH). Following the equation $\rho \propto \exp(T_0/T)^{1/1+D}$, with D being the dimensionality of the hopping processes, the data were analyzed. The resistivity of CeAgAs$_2$ gives a reliable agreement to the assumption of a 3D VRH over a wide temperature range (50–300 K) (N. B.: The 3D
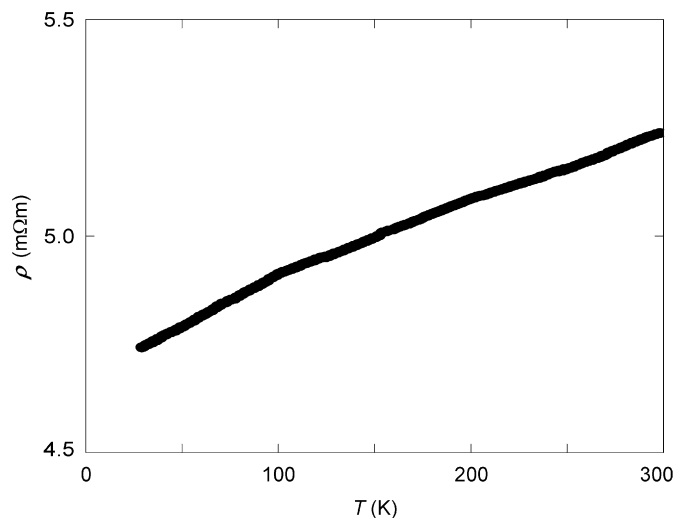
character may very well be the result of the polycrystalline nature of the samples). This behaviour could be a hint to Mott VRH at CeAgAs$_2$ at higher temperatures which vanishes at lower temperatures because the energy separation reduces the hopping probability. On the other hand, the conductivity of CeAuAs$_2$ which has much lower absolute resistivity values does not follow the hopping model and seems to be influenced mainly by temperature changes of the band structure caused by the structural modification.

The resistivities of two silver compounds increase linearly with increasing temperature indicating metallic conductivity for PrAgAs$_2$ (Fig. 13) and NdAgAs$_2$ (not shown here). This behavior is probably of general character in the LnAgAs$_2$ series (with exception of the La and Ce compounds) and comparable to the copper compounds LnCuAs$_2$ [43–46]. It should be conceded, that an influence of the grain boundaries of investigated pellets on the resistivities can not be excluded completely.

Total and partial calculated electronic densities of states (DOS) for LaAgAs$_2$ and PrAgAs$_2$ are presented in Fig. 14. Unfortunately, no self consistent result could be obtained for CeAgAs$_2$. Therefore, electronic properties have been calculated for LaAgAs$_2$ to use the iso-structural LaAgAs$_2$ as non-magnetic reference system to compare with the experimental results for the Ce compound. Total and partial calculated electronic densities of states (DOS) are presented in Fig. 14. The computed valence DOS is similar for both compounds, although the DOS for LaAgAs$_2$ is stronger structured due to the additional band splitting caused by the As distortion. In contrast to the experimental observation, metallic behavior is proposed for both compounds. On the other hand, a low DOS (pseudo gap) is found at the Fermi level. The pseudo gap for the La compound is a little more pronounced compared to the Pr system, reflecting the small additional lattice distortion. At the Fermi level, mainly contributions from As 4p electrons with a small admixture of Ag and the respective lanthanide element are found. The Ag 4d shell is mostly filled and rather low in energy (between −6 eV and −4 eV).

The band structures for both systems are shown in Fig. 15. Like in the DOS, the strong similarity of the compounds is reflected in their band structure. Since Pr has magnetic moments due to the 4f electrons, the bands are spin split. However, due to the localized character of the 4f electrons, this spin splitting is very small for the other valence electrons and negligible with respect to the band dispersion.

The presented resistivity data can be understood in connection to the crystal structure and the electronic band structure. Probably, the semiconducting behavior is favored in the *Pmca* compounds with cis-trans chains of As atoms, whereas the *Pmcn* systems with As zigzag chains disclose metallic conductivity. The results of the band structure calculations show that mainly the As states contribute to the (small) density of states at the Fermi level. In connection with the fact that the interatomic As–As distances are small, it can be concluded that the electronic transport is favored along the As chains. The character and size of the rare-earth ions influence the transport properties and may result in a structural modification.

In the DOS curves, the main difference between the two compounds $LaAgAs_2$ and $PrAgAs_2$ concerns $4f$ contribution. In both compounds, the unoccupied $4f$ states are found at about 2.5 eV, whereas the occupied $4f$ states of Pr are at about -5.5 eV. This is consistent with the applied U of 8 eV, which should be a measure for the split between the occupied and the unoccupied the $4f$ states.

For the band structures, the bands crossing the Fermi level and being responsible for the metallic character have a typical band width of about 2 eV. This rather large band width is most likely also the reason, why no insulating behavior despite the additional lattice distortion is found for the La compound. Only in one part of the k-space, namely between Z and T (see Fig. 15) the bands split around the Fermi level.

One possible explanation for the difference between experimental observation and calculation might be a segregation of arsenic in the grain boundaries of the pellets during the compression or sintering, which could account for the measured semiconducting behavior of some compounds. Another explanation might be a different conducting behavior of the iso-structural $LaAgAs_2$ (calculation) and $CeAgAs_2$ (measurement).

3.3. Magnetization experiments

From the $LnTAs_2$, the samples with Ln=Pr, Nd, Sm and T=Ag, Au were studied for their magnetic behavior. For comparison, the copper samples $PrCuAs_2$ and $SmCuAs_2$, prepared under identical conditions as outlined in Section 2.1, were added. Hysteresis measurements at room temperature confirm the paramagnetic nature for all compounds. Most samples develop an antiferromagnetic ordering at low temperature. As an example, Fig. 16 shows the normalized magnetic moments m for the $PrTAs_2$ samples (T=Cu, Ag, Au).

$PrCuAs_2$ undergoes an antiferromagnetic ordering at $T_N \approx 4.5$ K, which shows up in the peak of the $m(T)$ curve (Fig. 16a). The inverse susceptibility $\chi^{-1} = \mu_0 H/m$ (inset), with m being the mass-normalized magnetic moment in emu/g, is perfectly linear between 10 and 300 K and intersects the temperature axis at $\theta = -5$ K. A field dependent measurement at 2.5 K (i.e. below T_N), however, shows a slightly kinked hysteresis, characteristic of a metamagnetic transition at a critical field of about 0.3 T (Fig. 16b). Such a field induced transition into a ferromagnetic ordered state
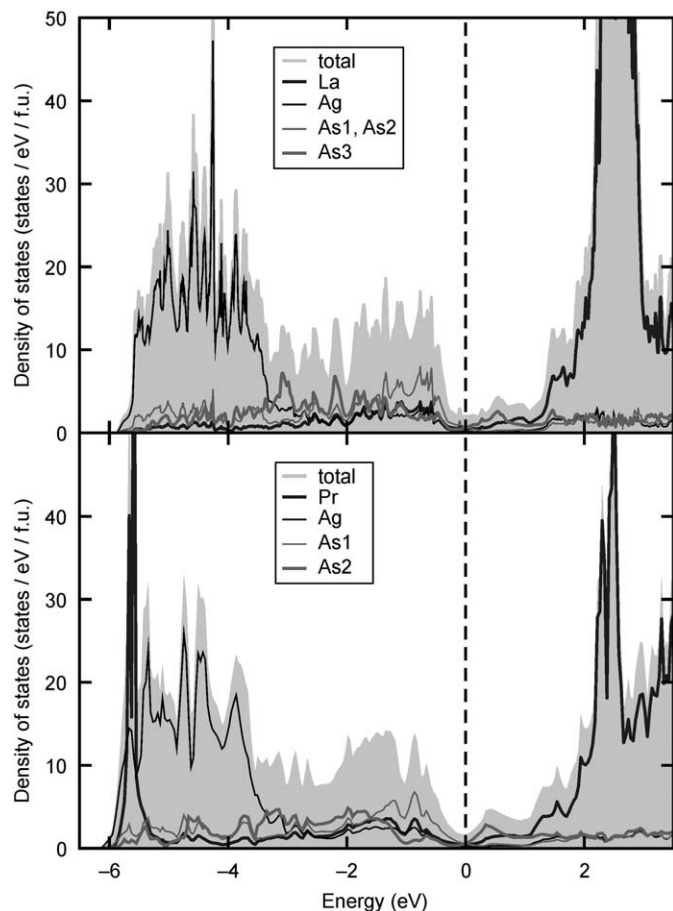

Fig. 14. Total and partial electronic DOS for $LaAgAs_2$ (upper panel) and $PrAgAs_2$ (lower panel). The Fermi level is set to zero.
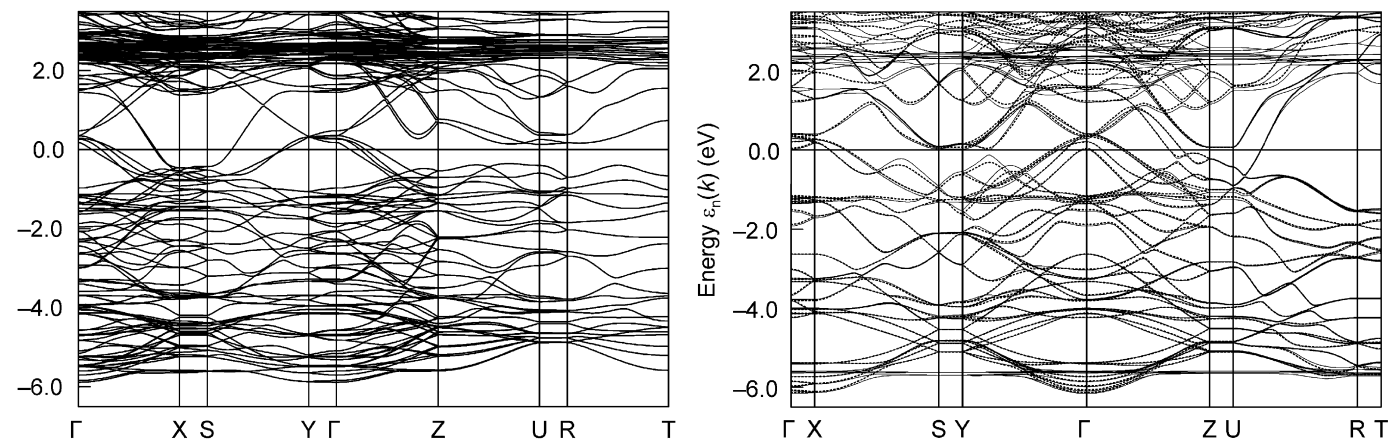

Fig. 15. Band structure of $LaAgAs_2$ (right panel) and $PrAgAs_2$ (left panel). For $PrAgAs_2$, the two spin directions are indicated by full and dashed lines, respectively. The Fermi level is set to zero.
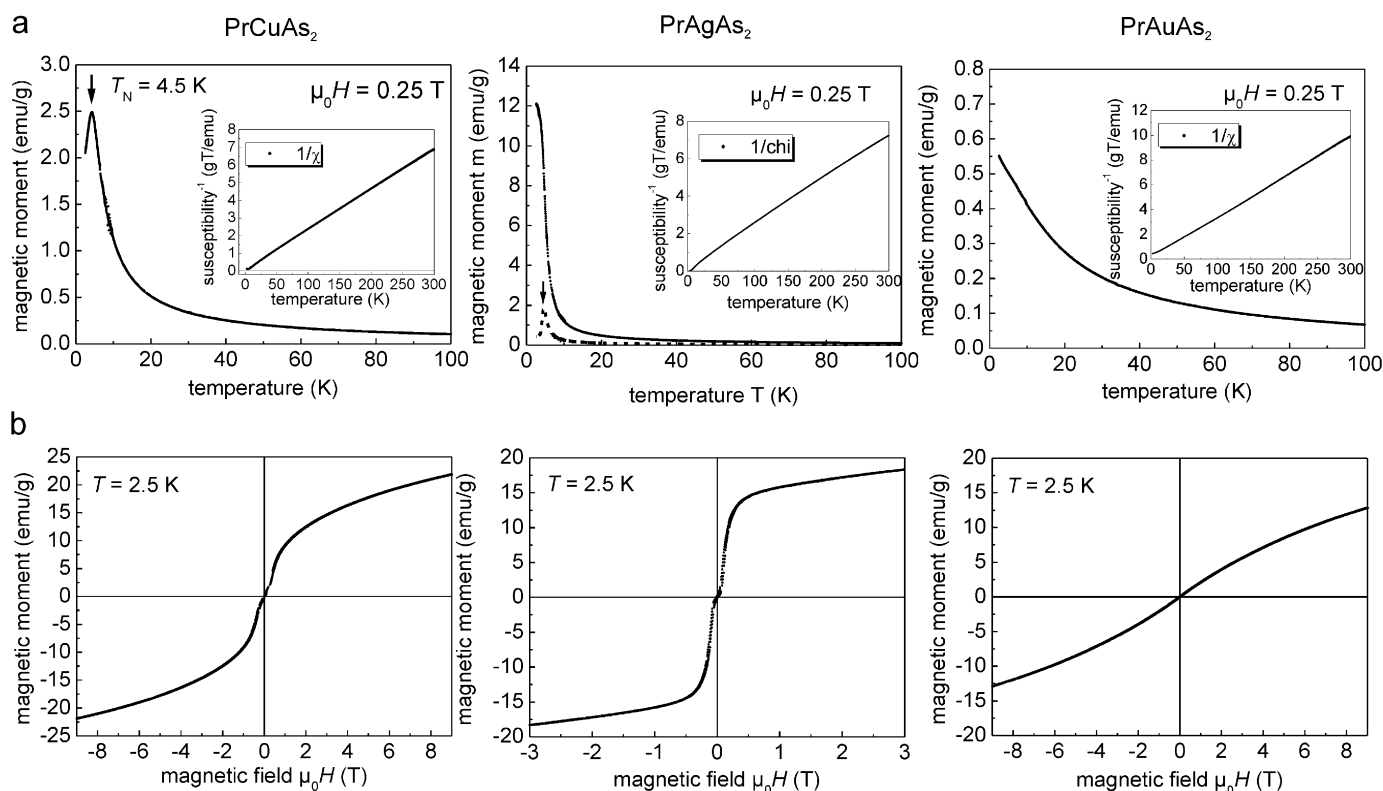
Fig. 16. Magnetic properties of PrTAs$_2$ compounds with T=Cu, Ag and Au. (a) Normalized temperature dependent magnetic moment m measured at a fixed field of $\mu_0 H$=0.25 T together with the inverse susceptibility χ^{-1}=$\mu_0 H/m$ as a function of temperature (inset). For PrAgAs$_2$, $m(T)$ has been measured additionally at $\mu_0 H$=0.01 T (dashed curve) and is multiplied by a factor 5 for better visibility. (b) Normalized magnetic moment m as a function of applied field for constant temperature T=2.5 K.

has already been observed for CeAgAs$_2$ [21] and appears for several other LnTAs$_2$ compounds, which order antiferromagnetically. PrAgAs$_2$ shows a very similar behavior, however with a metamagnetic transition below 0.1 T (see hysteresis at 2.5 K in Fig. 16b). Consequently, the $m(T)$ curve measured at 0.25 T resembles that of a ferromagnetic material with a strong increase of magnetic moment below 10 K. In order to reveal the antiferromagnetic ground state, $m(T)$ has been measured additionally in a field of 0.01 T. The peak indicates a Néel temperature of $T_N \approx 4.6$ K (see arrow). The inverse susceptibility is linear in the temperature range from 50 to 300 K. The third praseodymium compound, PrAuAs$_2$, shows a purely paramagnetic behavior down to a temperature of 2 K, seen in both the $m(T)$ and $m(H)$ measurements. χ^{-1} is again perfectly straight as expected for paramagnetic ordering. Antiferromagnetic coupling below 2 K cannot be excluded, and the negative extrapolated intersection of χ^{-1} with the temperature axis supports this assumption.

The slope C^{-1} of χ^{-1} can be compared with the theoretical Curie–Weiss behavior expected from the single ion moment of Pr^{3+}.

$$C = \frac{J(J+1)(g_L\mu_B)^2 n}{3k_B} \quad (1)$$

with J=4, g_L=Landé factor=4/5, n=number of ions per sample weight, μ_B=Bohr magneton and k_B=Boltzmann constant.

The experimentally found values of C=30.1 emu K g^{-1} T^{-1}, 41.4 emu K g^{-1} T^{-1} and 42.8 emu K g^{-1} T^{-1} fit very well with the expected values of C=31.5 emu K g^{-1} T^{-1}, 39.8 emu K g^{-1} T^{-1} and 44.8 emu K g^{-1} T^{-1} calculated from Eq. (1) for PrCuAs$_2$, PrAgAs$_2$ and PrAuAs$_2$, respectively. This confirms that the magnetism in these samples is dominated by the localized moments of the Pr^{3+} ion.
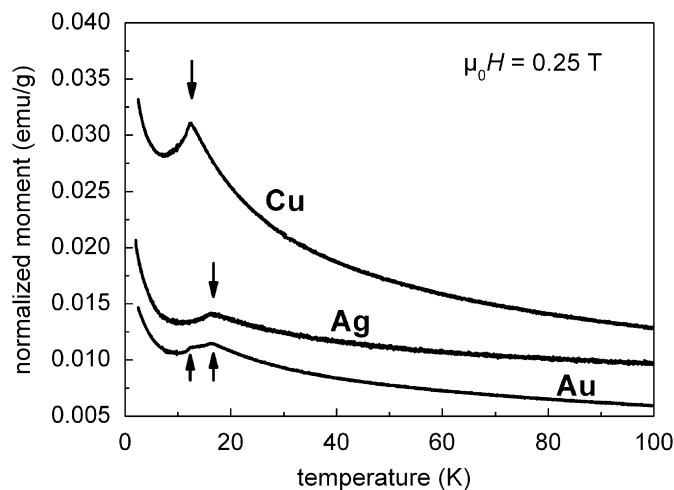

Fig. 17. Normalized magnetic moment m of the SmTAs$_2$ compounds (T=Cu, Ag, Au) as a function of temperature measured at a constant field of $\mu_0 H$=0.25 T. The peaks indicating an antiferromagnetic ordering temperature are marked by arrows.

Fig. 17 displays the temperature dependent, normalized magnetic moments for SmTAs$_2$ (T=Cu, Ag, Au). Due to the small total angular momentum number J=5/2 and Landé factor g_L=2/7 of the trivalent Sm^{3+}, the normalized moment is considerably smaller than for the Pr samples. All three curves show distinct peaks, which indicate an antiferromagnetic ordering at low temperatures. Field dependent hysteresis loops at 2.5 K (not shown here) do not exhibit any sign of a metamagnetic transition. It is interesting to note that in SmAuAs$_2$ two transitions

temperatures are observed, which coincide with the individual ordering temperatures of $T_N = 12.4$ and 17 K of SmCuAs$_2$ and SmAgAs$_2$, respectively.

The remaining studied compounds, NdAgAs$_2$ and NdAuAs$_2$ also show antiferromagnetic order without metamagnetic transitions and with *Néel* temperatures of $T_N = 2.7$ and 3.4 K, respectively. As in the case of PrAuAs$_2$, the effective moment of NdAuAs$_2$ in the paramagnetic state is compatible with the magnetic configuration of the isolated Nd^{3+} ions.

4. Conclusions

The structures of the lanthanide coinage-metal diarsenides *Ln*TAs$_2$ (*Ln* = La, Ce–Sm; *T* = Ag, Au) have been reinvestigated and refined from single crystal data. Two different ordered distortion variants of the HfCuSi$_2$ type are presented, with the As atoms of the planar layer forming either cis-trans or zigzag chains due to *Peierls*-like distortions. The distortions were also found for compounds which have previously been described in the subcell of the undistorted aristotype. The space groups were derived via group-subgroup relations.

From the band structure calculations it is found that the small additional structural distortion in the La compound has only minor influence on the As states at Fermi level and is not large enough to cause insulating behavior. Therefore it remains an open question whether or not the observed metallic behavior is really intrinsic.

All *Ln*TAs$_2$ compounds exhibit different magnetic ordering depending on the lanthanide and coinage-metal species. All samples are paramagnetic at room temperature and all studied compounds but PrAuAs$_2$ show magnetic ordering between 2 and 20 K. In most cases the effective moment in the paramagnetic state is explained by the magnetic configuration of the trivalent lanthanide ion. NdTAs$_2$ (*T* = Ag, Au) and SmTAs$_2$ (*T* = Cu, Ag, Au) order antiferromagnetically without a hint for a metamagnetic transition, whereas PrTAs$_2$ (*T* = Cu, Ag) adopts ferromagnetic ordering above a small critical field.

One possible explanation for the difference between experimental and computed transport properties might be the influence of grain boundaries and a possible segregation of arsenic for some compounds. Thus, new experiments on single crystals would be highly desirable, especially as a strong anisotropy of the electrical conductivity can be expected.

References

[1] B. Eisenmann, N. May, W. Müller, H. Schäfer, A. Weiss, J. Winter, G. Ziegleder, Z. Naturforsch. 25 (1970) 1350–1352.
[2] B. Eisenmann, N. May, W. Müller, H. Schäfer, Z. Naturforsch. 27b (1972) 1155–1157.
[3] E. Brechtel, G. Cordier, H. Schäfer, Z. Naturforsch. 35b (1979) 1–3.
[4] C. Zheng, R. Hoffmann, J. Am. Chem. Soc. 108 (1986) 3078–3088.
[5] G. Venturini, B. Malaman, B. Roques, J. Solid State Chem. 79 (1989) 126–135.
[6] G. Venturini, B. Malaman, B. Roques, J. Solid State Chem. 79 (1989) 136–145.
[7] S.I. Chykhrij, G.V. Loukasouk, S.V. Oryshchyn, Yu. Kuz'ma, J. Alloys Comp. 248 (1997) 224–232.
[8] M. Wang, B. McDonald, A. Mar, J. Solid State Chem. 147 (1999) 140–145.
[9] L.S. Andrukhiv, L.A. Lysenko, Ya.P. Yarmolyuk, E.I. Gladyshevskii, Dop. Akad. Nauk Ukr. RSR, Ser. A (1975) 645–648.
[10] O. Sologub, K. Hiebl, P. Rogl, H. Noël, O.I. Bodak, J. Alloys. Comp. 210 (1994) 153–157.
[11] O. Sologub, K. Noël, A. Leithe-Jasper, P. Rogl, O.I. Bodak, J. Solid State Chem. 115 (1995) 441–446.
[12] M. Brylak, M.H. Möller, W. Jeitschko, J. Solid State Chem. 115 (1995) 305–308.
[13] Yu. Mozharivskyj, D. Kaczorowski, H.F. Franzen, J. Solid State Chem. 155 (2000) 259–272.
[14] Yu. Mozharivskyj, D. Kaczorowski, H.F. Franzen, Z. Anorg. Allg. Chem. 627 (2001) 2163–2172.
[15] R.O. Demchyna, Yu.B. Kuz'ma, V.S. Babizhetsky, J. Alloys Comp. 315 (2001) 158–163.
[16] M. Kolenda, A. Oles, A. Szytula, J. Alloys Comp. 322 (2001) 55–58.
[17] Yu. Mozharivskyj, V.K. Pecharsky, H.F. Franzen, J. Alloys Comp. 345 (2002) 100–104.
[18] J.P. Jemetio, Th. Doert, O. Rademacher, P. Böttcher, J. Alloys Comp. 338 (2002) 93–98.
[19] J.P. Jemetio, T. Doert, P. Böttcher, Z. Kristallogr. NCS 217 (2002) 455–457.
[20] M. Eschen, W. Jeitschko, Z. Naturforsch. 58b (2003) 399–409.
[21] R. Demchyna, J.P.F. Jemetio, Yu. Prots, Th. Doert, L.G. Akselrud, W. Schnelle, Yu. Kuz'ma, Yu. Grin, Z. Anorg. Allg. Chem. 630 (2004) 635–641.
[22] Y. Kamihara, H. Hiramatsu, M. Hirano, R. Kawamura, H. Yanagi, T. Kamiya, H. Hosono, J. Am. Chem. Soc. 128 (2006) 10012–10013.
[23] Y. Kamihara, T. Watanabe, M. Hirano, H. Hosono, J. Am. Chem. Soc. 130 (2008) 3296–3297.
[24] T. Watanabe, H. Yanagi, T. Kamiya, Y. Kamihara, H. Hiramatsu, M. Hirano, H. Hosono, Inorg. Chem. 46 (2007) 7719–7721.
[25] F. Hunte, J. Jaroszynski, A. Gurevich, D.C. Larbalestier, R. Jin, A.S. Sefat, M.A. McGuire, B.C. Sales, D.K. Christen, D. Mandrus, Nature 453 (2008) 903–905.
[26] V. Johnson, W. Jeitschko, J. Solid State Chem. 11 (1974) 161–166.
[27] WinXPow, Program for the collection and the evaluation of x-ray powder data, Stoe & Cie. GmbH, Darmstadt, 1999.
[28] XRed32, Data reduction program, Stoe & Cie. GmbH, Darmstadt, 2001.
[29] XShape, Crystal optimisation for numerical absorption correction program, Stoe & Cie. GmbH, Darmstadt, 1999.
[30] G.M. Sheldrick, SHELX97—Program for crystal structure determination, University of Göttingen, Germany, 1997.
[31] K. Koepernik, H. Eschrig, Phys. Rev. B 59 (1999) 1743–1757.
[32] I. Ophale, K. Koepernik, H. Eschrig, Phys. Rev. B 60 (1999) 14035–14041.
[33] J.P. Perdew, Y. Wang, Phys. Rev. B 45 (1992) 13244–13249.
[34] M.T. Czyzyk, G.A. Sawatzky, Phys. Rev. B 49 (1994) 14211–14228.
[35] H. Eschrig, K. Koepernik, I. Chaplygin, J. Solid State Chem. (2003) 482–495.
[36] V.I. Anisimov, J. Zaanen, O.K. Andersen, Phys. Rev. B 44 (1991) 943–954.
[37] A.I. Liechtenstein, V.I. Anisimov, J. Zaanen, Phys. Rev. 52 (1995) R5467–R5470.
[38] H. Bärnighausen, Match 9 (1980) 139–175.
[39] T. Hahn, A.J.C. Wilson (Eds.), International Tables for Crystallography, fourth ed., vol. A, Kluwer Academic Publishers, Dordrecht, 1996.
[40] D. Rutzinger, Th. Doert, M. Ruck, Acta Cryst. B 65 (2009) 527–534.
[41] B. Cordero, V. Gómez, A.E. Platero-Prats, M. Revés, J. Echeverría, E. Cremades, F. Barragán, S. Alvarez, Dalton Trans. (2008) 2832–2838.
[42] D. Rutzinger, C. Bartsch, Th. Doert, M. Ruck, Acta Cryst. B 65 (2009) 519–526.
[43] E.V. Sampathkumaran, T. Ekino, R.A. Ribeiro, K. Sengupta, T. Nakano, M. Hedo, N. Fujiwara, M. Abliz, Y. Uwatoko, S. Rayaprol, Th. Doert, J.P. Jemetio, Physica B 359–361 (2005) 108–110.
[44] M. Szlawska, D. Kaczorowski, J. Alloys Comp. 451 (2008) 464–466.
[45] E.V. Sampathkumaran, K. Sengupta, S. Rayaprol, K.K. Iyer, Th. Doert, J.P.F. Jemetio, Phys. Rev. Lett. 91 (2003) 36603/1–4.
[46] K. Sengupta, S. Rayaprol, E.V. Sampathkumaran, Th. Doert, J.P.F. Jemetio, Physica B 348 (2004) 465–474.